





Shear band formation during nanoindentation of EuB_6 rare-earth hexaboride

Rajamallu Karre¹, Yidi Shen², Shuangxi Song ¹, Yixuan Hu¹, Simanta Lahkar ¹, Xiaodong Wang¹, Qi An ² & Kolan Madhav Reddy ¹✉

Research on rare-earth hexaborides mainly focuses on tuning their electronic structure from insulating-to-metallic states during high pressure experiments. However, the structural evolution that contributes to their mechanical failure is not well understood. Here, we examine the pressure-induced structural evolution of a model rare-earth hexaboride, EuB_6 , during nanoindentation. Transmission electron microscopy reveals that nanoscale amorphous shear bands, mediated by dislocations, play a decisive role in deformation failure. Density functional theory calculations confirm that amorphous bands evolve by breaking boron-boron bonds within B_6 octahedra during shear deformation. Our results underscore an important damage mechanism in hard and fragile hexaborides at high shear pressures.

¹State Key Laboratory of Metal Matrix Composites, School of Materials Science and Engineering, Shanghai Jiao Tong University, 200240 Shanghai, China.

²Department of Chemical and Materials Engineering, University of Nevada-Reno, Reno, NV 89557, USA. ✉email: kmreddy@sjtu.edu.cn

Rare-earth hexaborides (RB_6) have attracted considerable attention due to their extraordinary combination of electrical, magnetic, thermal, and mechanical properties¹. At ambient conditions, RB_6 crystallizes in a cubic structure (i.e., CsCl-prototype, Space group: $Pm\bar{3}m$ (no: 221))². The unique chemical bonding in RB_6 arises from the octahedron B_6 framework with large interstitial space to host a variety of the rare earth ions ($R=\text{Ba, Ce, Eu, La, Sm, Sr, Y}$ etc.) at the center of cubic crystal lattice. Despite having the same crystal structure, the properties of each hexaboride are uniquely different and diversified from each other due to their intrinsically strong correlated electron systems³. For instance, CeB_6 shows dense Kondo effect and electric quadrupole ordering⁴, SmB_6 exhibits Kondo insulating and valence fluctuation⁵, LaB_6 have low work function for thermionic emission⁶, YB_6 possess remarkable superconductivity⁷, CaB_6 is semiconducting⁸, and EuB_6 displays ferromagnetic properties^{1,3}.

Pressure-induced polymorphism in several hexaborides has been predicted and observed by first-principle calculations and high-pressure X-ray experiments^{9–12}. For instance, Kolmogorov et al.⁹ predicted that the thermodynamically unstable cubic ($Pm\bar{3}m$) CaB_6 structure at high pressure compression transforms to an intermediate metastable orthorhombic $oS28$ structure around 13 GPa before stabilizing to ground state tetragonal $tI56$ structure above 32 GPa. Their experimental evidence showed $Pm\bar{3}m$ structure in three-dimensional morphology remains stable up to at least 28 GPa but with certain distortion. Further, assistance of laser heating promoted the rebonding in strong covalent boron network above 31 GPa and favored the ground state structure. Zhu et al.¹⁰ examined a semiconducting SrB_6 ($Pm\bar{3}m$) and predicated new metallic polymorphs as orthorhombic ($Cmmm$) and tetragonal ($I4/mmm$) structures at high pressure of 48 and 60 GPa, respectively. These unique boron polyhedra are formed as a result of denser structural arrangement under high pressure and the formation enthalpies are decreased due to the additional B-B bonds of polyhedral networks¹⁰. In addition, they have also demonstrated a novel deformation mechanism with transient multicenter bonding yields in good combination of high strength and high ductility for the $I4/mmm$ structure in SrB_6 ¹⁰. Cooley et al. performed high pressure measurements and found that ferromagnetic order of EuB_6 was driven by the Ruderman-Kittel-Kasuya-Yosida interaction between Eu moments and pockets of semimetallic conduction electrons¹³. Further, high pressure compression studies of CeB_6 confirmed that there is no volume dependency on dense Kondo behavior and also found no trace of first and second-order transitions up to 20 GPa¹⁴. Besides, previous experimental studies in hexaborides are predominantly conducted to determine the mechanical properties (Young's modulus and hardness)^{15,16}. A study by Dub et al.¹⁶ using nanoindentation experiment on a single crystal LaB_6 showed elastic-to-plastic (pop-in) transition as an indication of dislocations but was not provided direct evidence of this associated high-pressure phase transitions. These researchers suggest that high pressure produces the complex boron networks and structural transformations in hexaborides leading to unique properties, which has created immense interest for electro-mechanical systems applications^{3,9–14}.

Here, we choose EuB_6 firstly because of its semi-metallic nature and its hardness (19–26 GPa) falling in range of CaB_6 (16–28 GPa) and SrB_6 (18.5–27 GPa)¹⁷. Moreover, compressibility of EuB_6 is also comparable with that of LaB_6 in the pressure range of 0–8 GPa¹⁸. Secondly, EuB_6 is the only hexaboride with ferromagnetic order and low thermal expansion coefficient, which can be tuned to ground state electron system^{3,13}. Thirdly, single-phase EuB_6 in bulk material can be easily produced using various sintering methods^{2,19,20}. In addition to these applications, EuB_6

received significant attention in hexaboride family as a potential second phase material for structural applications owing to its high thermal stability and high neutron absorption properties^{19,21}.

In this study, we used nanoindentation to impose high pressures on EuB_6 crystals, followed by microstructural characterization using Raman spectroscopy and spherical aberration (Cs) corrected transmission electron microscopy (TEM). We found beneath the indentation surface, the nanoscale amorphous shear bands preceded by the emission and propagation of dislocations. The density functional theory (DFT) simulations, which agree with experiment, reveals that the chemical bond breaking within octahedral B_6 initiates the mechanical instability leading to the localized amorphization in EuB_6 by high pressure shear deformation.

Results

Structure characterization of as-synthesized EuB_6 . The microstructure of as-synthesized EuB_6 -boron carbide (B_4C) composite is shown in Fig. 1. In Fig. 1a scanning electron microscopy (SEM) image shows the bright grains having faceted cuboidal corresponding to EuB_6 crystals which are surrounded by the gray region of B_4C matrix. Figure 1b electron back scattered diffraction (EBSD) pattern of EuB_6 acquired from the same region of Fig. 1a, displays the crystallographic orientation for the grain facets. Inset of Fig. 1b shows an inverse pole figure (IPF) map for EuB_6 grains confirm that the grain shapes of square, rectangle and triangle correspond to (100), (110) and (111) crystal orientations with color code as red, green and blue, respectively. High-resolution TEM (HRTEM) images of EuB_6 are projected along the [100] and [120] zone axes in Fig. 1c, d as confirmed by selected area electron diffraction (SAED) patterns shown in the inset at the upper right corner of Fig. 1c, d. Further, simulated atomic images projected along the same zone axes are superimposed at the lower right corner of the HRTEM images (Fig. 1c, d). The comparison of experimental and simulated TEM images (Fig. 1c, d) reveals that the bright spots belong to europium (Eu) individual atomic sites and gray spots are corresponding to the boron (B_6) clusters, where Eu and B atoms are represented by open circles with magenta and green colors, respectively.

Raman Spectroscopy of pristine and deformed EuB_6 . In order to determine the mechanical properties and introduce structural transformations in EuB_6 crystals, we performed nanoindentation on different facets of EuB_6 with a maximum load of 10 mN which is well below the load for pop-in events (Supplementary Note 1 and Supplementary Fig. 1). The measured hardness and elastic modulus for (100), (110), and (111) facets are 28.52 ± 0.42 GPa, 28.88 ± 0.72 GPa, 27.72 ± 1.05 GPa and 231 ± 2.5 GPa, 240 ± 5 GPa, 225 ± 8.7 GPa, respectively. The representative images before and after nanoindentation using optical microscope and Scanning Probe Microscope (SPM) as shown in Supplementary Fig. 2a–c. A load-depth curve is shown in Supplementary Fig. 2d with the applied load of 10 mN penetrating to a maximum depth of 130 nm, which is well below 10% of the thickness of EuB_6 crystals. When the load is increased gradually to ~ 70 mN, abrupt discontinuity in load-depth curve (i.e., pop-in) observed at about ~ 12 mN (Supplementary Fig. 3) in the EuB_6 of (001) surface. The pop-in phenomenon in crystalline materials are often related to nucleation and propagation of dislocations or twinning along a specific slip system or cleavage cracks in certain crystallographic plane^{16,22,23}. Figure 2a shows the representative SEM image of residual indentation impression produced on the grain of square ((001) orientation) facet at applied load of ~ 70 mN. The Raman spectra acquired from the residual indent (black solid line) and pristine (red dotted line) of

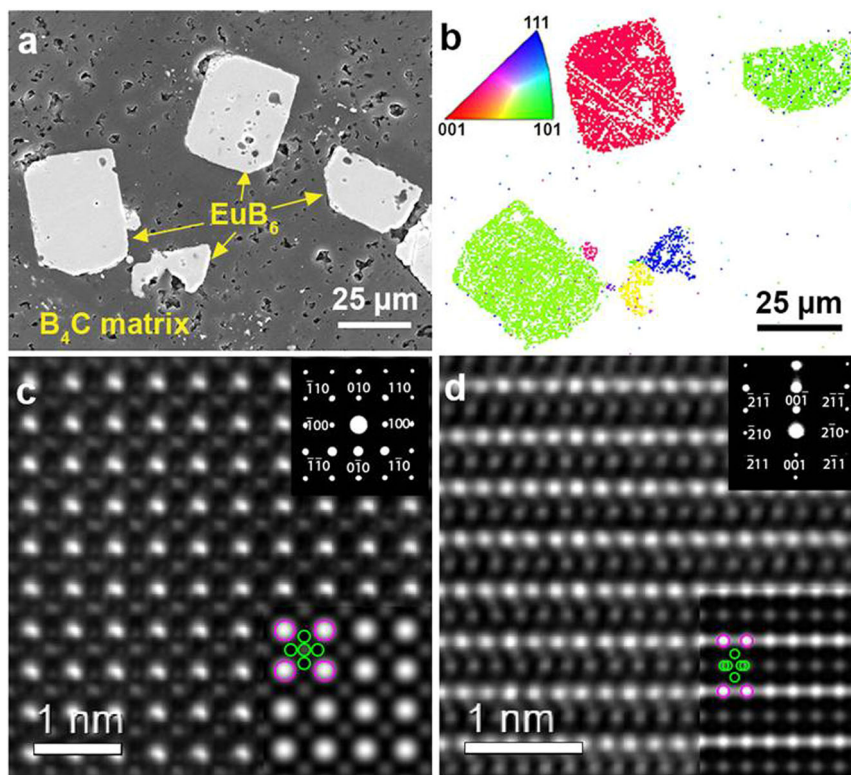


Fig. 1 Electron microscopy characterization of as-synthesized EuB_6 . **a** Secondary electron SEM image shows microstructure of EuB_6 - B_4C composite. **b** Corresponding EBSD pattern of EuB_6 phase. **c** and **d** High-resolution TEM images of EuB_6 along $[100]$ and $[120]$ zone axes, respectively. Simulated HRTEM images are superimposed on the rightmost lower corner of the images. The boron (B) and europium (Eu) atoms are represented by open circles with green and magenta colors, respectively. The indexed diffraction patterns along same zone axes are also shown at the rightmost upper corner of the images.

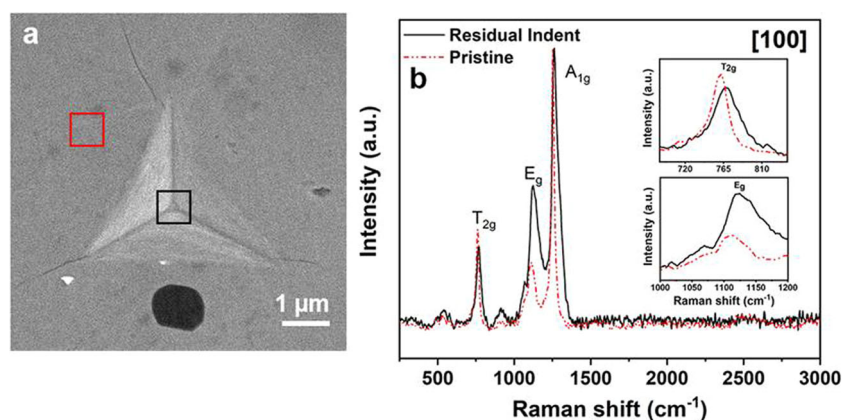


Fig. 2 Raman spectroscopy characterization of pristine and deformed EuB_6 . **a** SEM image shows Berkovich-indentation impression at applied of 70 mN on square cuboid ($[100]$ orientation) of EuB_6 . Here, the square boxes illustrate the regions from which the micro-Raman spectra acquired; black and red boxes represent the residual indent and pristine regions, respectively. **b** Raman spectra of EuB_6 from residual indent (black line) and pristine (red-dotted line) regions show three major peaks T_{2g} (768 cm^{-1}), E_g (1112 cm^{-1}), and A_{1g} (1256 cm^{-1}). The enlarged view for T_{2g} and E_g are given in the inset.

EuB_6 are presented in Fig. 2b. Since EuB_6 belongs to the cubic O_h group, there are three Raman active (T_{2g} , E_g , and A_{1g}) phonons caused by internal displacement of boron atoms in the octahedron B_6 ²⁴. In this study, these characteristic peaks are found at 768 cm^{-1} , 1112 cm^{-1} , and 1256 cm^{-1} , respectively, which are in good agreement with the previous reports^{11,20}. All the Raman peaks in Fig. 2b are related to the vibrations of octahedral B_6 . The E_g mode is associated with compressing up and down vibrations, while T_{2g} mode is related to the scissoring displacement of B atoms in the octahedral B_6 ²⁵. Therefore, both T_{2g} and E_g modes are modulating the B-B-B bond angles, whereas, A_{1g} mode is

related to the stretching of B-B bond²⁵. From residual indent (Fig. 2b), peak broadening of T_{2g} and E_g peaks is apparent suggesting that the structural transformations in EuB_6 may have occurred in B-B-B bonds of octahedra B_6 sites upon indentation induced high pressures.

Structural evolution observations of indentation-induced EuB_6 . In order to elucidate the underlying mechanism which drives the structural transformations in EuB_6 during high pressure deformation, cross-sectional TEM specimens from multiple

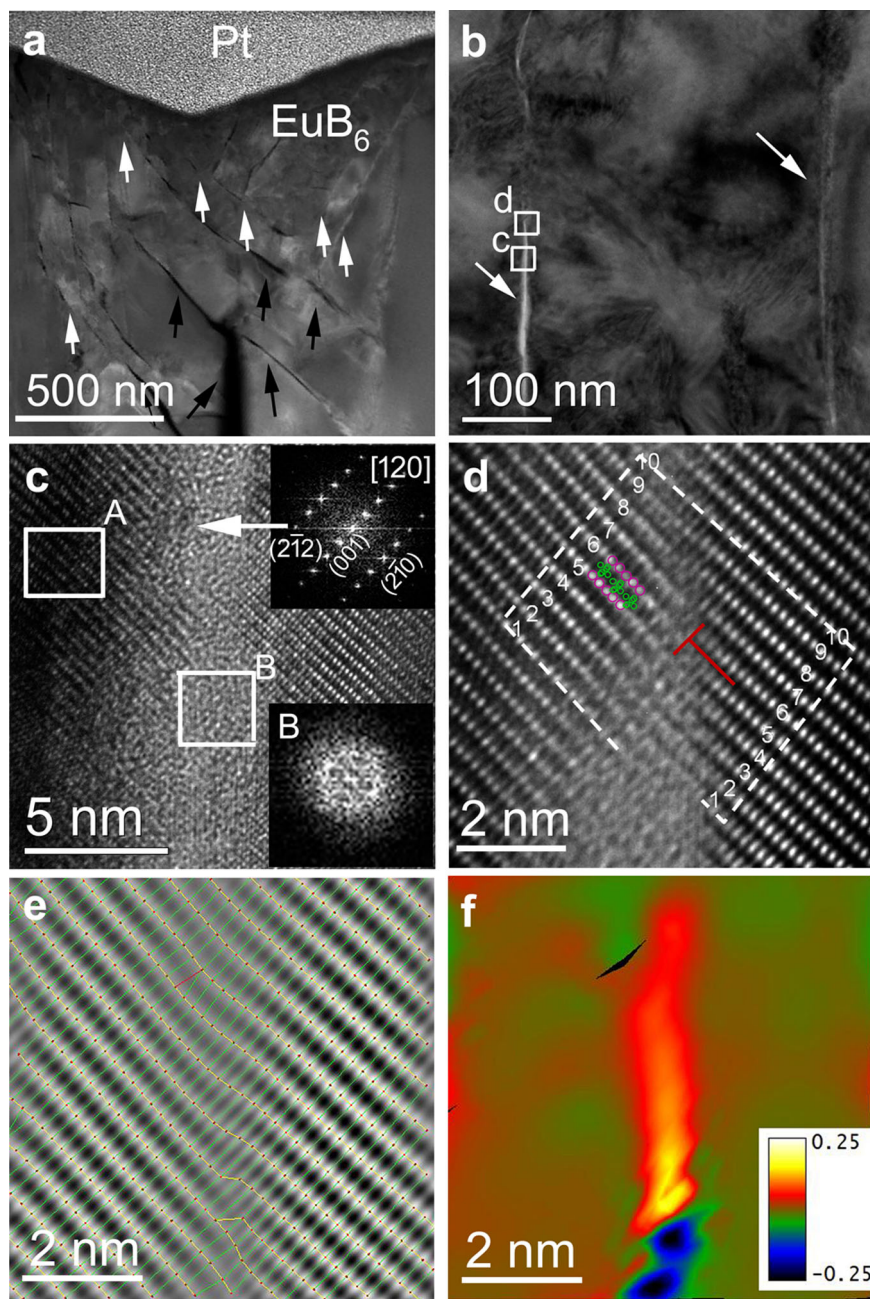


Fig. 3 TEM observations underneath the indent region along [100] orientation of EuB_6 . **a** Low magnification HAADF-STEM image of indent region shows microcracks and shear bands indicated by black and white arrows. **b** Magnified TEM image of shear bands with a length of ~ 300 nm. **c** High magnification TEM image shows the amorphous structure of the shear band with a width of 3 nm along the $(2\bar{1}2)$ plane. The FFT pattern of region A shows the crystallographic direction along $[120]$ direction and FFT pattern of region B demonstrate amorphous nature with diffuse halo ring of the shear band. **d** HRTEM image at the tip of the shear band shows emission of dislocations. The atomic overlay of Eu and B atoms on HRTEM shows a unit cell of EuB_6 in which atomic colors are consistent with Fig. 1. **e** Grid obtained by Peak Pair Analysis from the image shown in **d**. **f** shear strain (ϵ_{xy}) map obtained from same region of **e**.

crystallographic orientations were prepared from the residual indents using focused ion beam (FIB) milling^{26,27} (Fig. 3 and Supplementary Note 2, and Supplementary Fig. 4). Figure 3a shows high angle annular dark field (HAADF)-scanning TEM (STEM) image of indentation impression made on the (001) surface of EuB_6 cuboidal square at the maximum load of 70 mN (Supplementary Fig. 3). The microcracks and nanoscale bands (marked with dark and white arrow heads, respectively in Fig. 3a) can be seen from low magnification STEM image along the $[120]$ crystallographic direction, indicating severe damage and plastic

deformation take place beneath the indentation region. In the image of Fig. 3a, microcracks show high contrast owing to complete separation by an opening between two-sides of a crystal. Shear bands (in Fig. 3a, b) have much low contrast and have a width of ~ 3 –8 nm and length of 100–500 nm. Separate STEM-EDS maps (Supplementary Fig. 5) obtained from residual indent confirm only elements of Eu and B without any platinum deposition. Magnified TEM bright field (BF) and dark field (DF) images show the shear band but without voids and open gaps as shown in Supplementary Fig. 6. From high resolution TEM

(HRTEM) image of Supplementary Fig. 7, it appears that the shear band acts as runway for the cracks. The zoom-in HRTEM image acquired from the nanosized band reveal the loss of crystallinity (Fig. 3c). Fast Fourier transforms (FFT) taken from the region B, shows a diffuse halo without any diffraction spots, confirming the occurrence of amorphous structure within the band. On the other hand, FFT pattern taken from the crystalline structure on either side of band along the [120] crystallographic direction displays $Pm\bar{3}m$ symmetry of EuB_6 (Inset A). Further, HRTEM with FFTs pattern confirm the formation of amorphous band roughly aligned on a $(2\bar{1}2)$ plane. The measured angle between the (001) surface plane and $(2\bar{1}2)$ slip plane is about 48° suggesting that the amorphous bands are induced by high shear stresses. Figure 3d is the HRTEM image taken from tip of the amorphous band, as shown in white box of Fig. 3a. The Burgers loop from the tip of amorphous band drawn by white dotted lines in Fig. 3d reveals obvious shear atomic displacement of about $\sim 2 \text{ \AA}$. Moreover, Eu and B atomic overlay in Fig. 3d at near amorphous band providing evidence of crystal lattice deregister from the boron clusters, rather than Eu atoms. Figure 3e is the grid generated through the Peak Pair Analysis algorithm in the same area. The grid lines in image (Fig. 3e) clearly shows significant lattice bending before the initiation of dislocations at the tip of band. Analysis of shear strain (ϵ_{xy}) map from the area (Fig. 3e), specifically identifies a maximum absolute shear strain of about 25% (Fig. 3f) as estimated from the proximity of dislocation core in a nano-strained band region compared to the parent crystalline structure. We also characterized the indentation impression profuse on the (011) rectangle surface of EuB_6 (Supplementary Figs. 8 and 9). TEM characterization along the [311] and [111] zone axes (Supplementary Figs. 8a, b and 9a, b) show the nanosized amorphous bands are roughly aligned parallel to the $(\bar{1}12)$ plane. A HRTEM image obtained from the tip of amorphous band identifies the dislocation formation (Supplementary Figs. 8c and 9c). It is also observed that the amorphous bands are surrounded by the high-density planar defects (Supplementary Figs. 8a and 9a) and these defects are typically dislocations (Supplementary Fig. 9c). These observations indicate that the amorphous band formation and/or cleavage crack could be responsible for a visible pop-in in the load-displacement curve of EuB_6 (Supplementary Fig. 3). The localized amorphization correlates with shear deformation and appears to be associated with the dislocation formation in EuB_6 .

DFT prediction of shear amorphization in EuB_6 . Based on the TEM observations (Fig. 3 and Supplementary Figs. 8 and 9), we assumed that the $(2\bar{1}2)[120]$ and $(110)[\bar{1}\bar{1}0]$ are two possible slip systems to initiate the deconstruction of B_6 octahedra and formation of amorphous bands in EuB_6 . Hence, we applied pure shear deformation on EuB_6 along these two slip systems. The obtained shear-stress-shear-strain relationship is shown in Fig. 4a. The ideal shear strength along $(2\bar{1}2)[120]$ is 29.09 GPa, which is much lower than that (41.67 GPa) along $(110)[\bar{1}\bar{1}0]$. This suggests that $(2\bar{1}2)[120]$ is more plausible slip system, which agrees very well with the experimental observation. Then, we examined the deformation and failure mechanism of EuB_6 along $(2\bar{1}2)[120]$ slip system, as shown in Fig. 4b–f. The intact structure before shear is shown in Fig. 4b. It is worth noting that the structure is shown along “B” axis ($[\bar{1}01]$ direction) rather than “A” axis (shear direction of [120]) to better describe the failure mechanism. The atomic structure viewed along [120] direction is shown in Supplementary Fig. 10. As shear strain increases to 0.465, the B22-B32 bond between two octahedra is gradually stretched from original 1.68 Å to 2.15 Å without breaking, as

shown in Fig. 4c. When the shear strain continuously increases to 0.489, the B22-B32 bond is stretched to 2.26 Å and breaks, as shown in Fig. 4d. This bond breaking also slightly releases the shear stress from the maximum of 29.09 GPa to 28.29 GPa. Then, with the increase of shear strain, B22 and B32 atoms move far from each other, leading to further decrease of shear stress. In particular, at 0.514 shear strain, the distance between B22 and B32 atoms is 2.42 Å, as shown in Fig. 4e. Finally, at 0.539 shear strain, the B16-B28 bond in the octahedron is stretched from original 1.75 Å to 1.90 Å and breaks (Fig. 4f), initiating the deconstruction of octahedra, which agrees with the results in experiments. This structural failure further releases the shear stress to 5.33 GPa.

In addition to $(2\bar{1}2)[120]$, we also examined the failure mechanism of EuB_6 along $(110)[\bar{1}\bar{1}0]$, as shown in Supplementary Fig. 11. Supplementary Fig. 11a shows the intact structure. At 0.245 shear strain corresponding to the ideal shear strength, the B25-B32 connecting two nearby octahedra is gradually stretched from original 1.68 Å to 2.13 Å, as shown in Supplementary Fig. 11b. However, this bond is not broken. Then, at 0.263 shear strain, the B25-B32 bond is drastically stretched to 2.36 Å and breaks, as shown in Supplementary Fig. 11c. This bond breaking releases shear stress to 39.65 GPa. Next, with increase of shear strain, the B25 and B32 atoms is stretched far from each other, leading to the further release of shear stress. Particularly, at 0.297 shear strain, the distance of B25 and B32 atoms is 2.88 Å, as shown in Supplementary Fig. 11d. The corresponded shear stress also decreases to 27.01 GPa. The above results indicate that the failure mechanism of EuB_6 under ideal shear deformation arises from the breaking of B-B bonds which connect two nearby octahedra first and then the deconstruction of octahedra.

To mimic the complex stress condition in the indentation experiments, we also applied biaxial shear deformation along the plausible slip system of $(2\bar{1}2)[120]$. The shear-stress-shear-strain relationship of EuB_6 along $(2\bar{1}2)[120]$ is shown for biaxial shear deformation in Fig. 5. The shear strength is 23.31 GPa (Fig. 5a), which is lower than 29.09 GPa for pure shear deformation (Fig. 4a). The obtained failure mechanism is shown in Fig. 5b–f. The initial structure is shown in Fig. 5b. At 0.229 shear strain, the shear stress reaches to its maximum value of 23.31 GPa. The B35-B16 and B53-B23 bonds in octahedron are slightly stretched from original 1.75 Å to 1.78 Å and 1.82 Å, respectively, as shown in Fig. 5c. Then, when the shear strain continuously increases to 0.225, these bonds are further stretched to 1.88 Å for B35-B16 and 1.91 Å for B53-B23 and break, as shown in Fig. 5d. This bond breaking also releases the stress from 23.31 GPa to 15.71 GPa. As shear strain further increases to 0.296, the B53-B6 bond is gradually stretched to 1.92 Å, as shown in Fig. 5e. However, it does not break at this shear strain. Next, at 0.319 shear strain, the B53 atom is stretched out of octahedron and B6-B53 bond breaks, as shown in Fig. 5f. The deconstruction of octahedron releases the shear stress to 4.96 GPa. Therefore, the failure mechanism of EuB_6 under biaxial shear deformation arises from the B-B bond breaking within the octahedra. This deconstruction of octahedra will initiate the formation of amorphous shear in EuB_6 , which further verifies the observation in the experiments.

Under pure shear deformation, we observe some of the broken B-B bonds within the octahedra, which initiates the formation of amorphization in EuB_6 . Then, to illustrate the following crack formation observed in the experiments, we examined tensile deformation of the structure after failure under pure shear deformation. Here, the tensile deformation was performed along $[2\bar{1}2]$ direction which is perpendicular to the shear plane. The structures before tensile deformation (0 tensile strain) and after structural failure (0.09 tensile strain) are shown in Supplementary

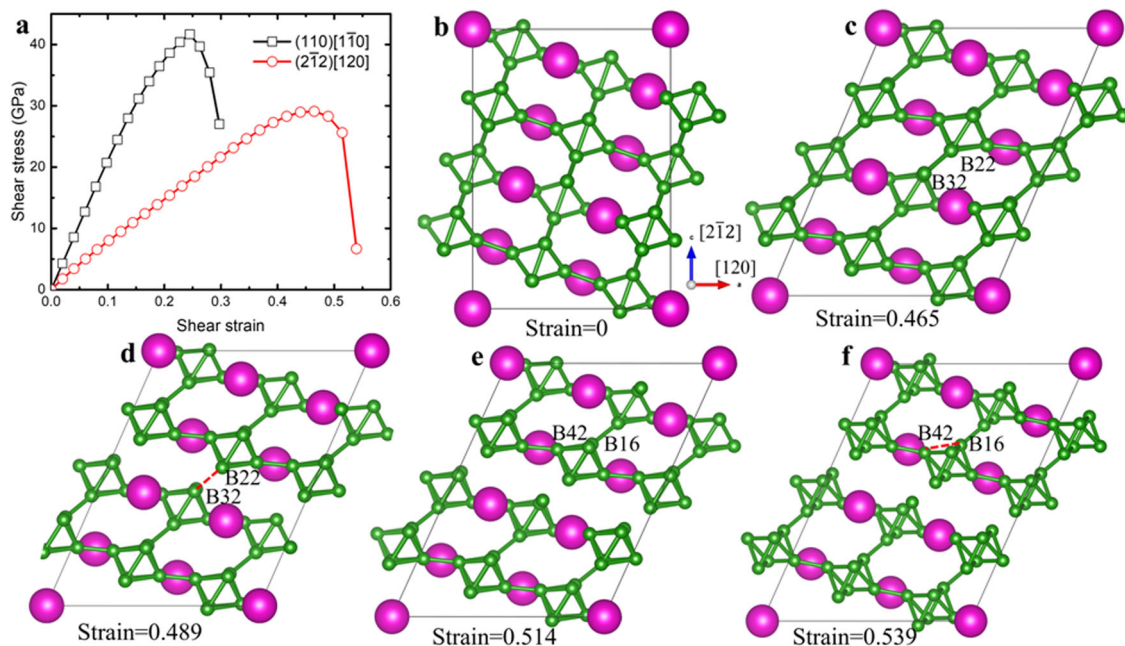


Fig. 4 The deformation and failure process of EuB_6 under pure shear deformation. **a** The shear-stress-shear-strain relationship along both $(2\bar{1}2)[120]$ and $(110)[\bar{1}\bar{1}0]$ slip systems. **b-f** The failure process along $(2\bar{1}2)[120]$: **b** the intact structure; **c** the structure at 0.465 strain before structural failure; **d** the structure at 0.489 strain in which B22-B32 bond breaks; **e** the structure at 0.514 strain; **f** the structure at 0.539 strain in which the B16-B42 bond breaks, initiating the deconstruction of octahedron. The green and magenta balls represent the B and Eu atoms, respectively.

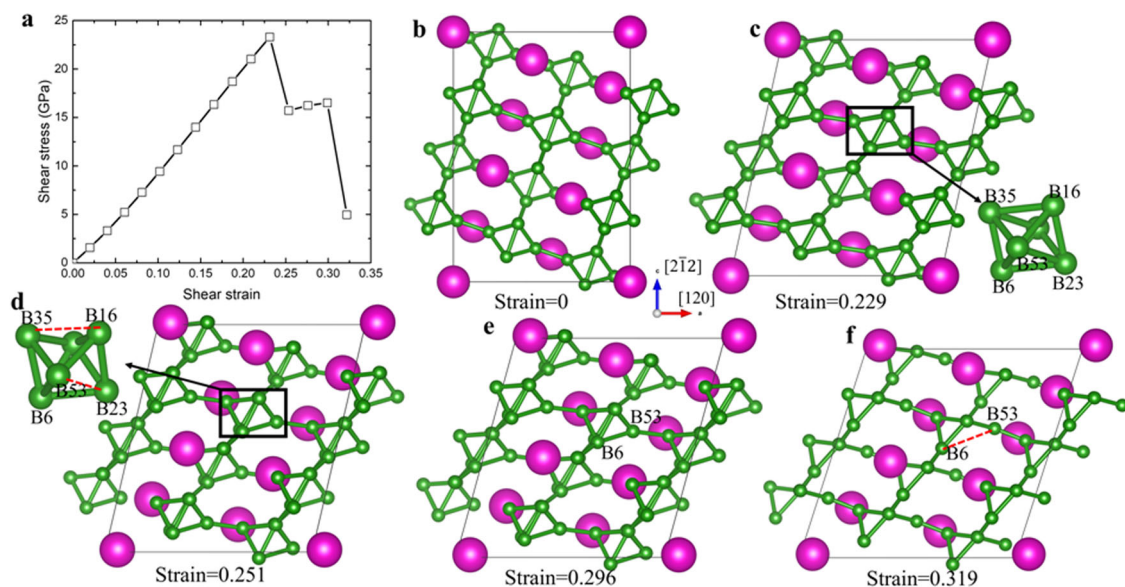


Fig. 5 The failure process of EuB_6 under biaxial shear deformation along $(2\bar{1}2)[120]$ slip system. **a** The shear-stress-shear-strain relationship. **b-e** The failure process: **b** the intact structure; **c** the structure at 0.229 strain with ideal strength; **d** the structure at 0.251 strain in which B35-B16 and B23-B53 bond within octahedron break; **e** the structure at 0.296 strain; **f** the structure at 0.319 strain after structural failure. The B53-B6 bond within octahedron breaks.

Fig. 12. At 0.09 tensile strain, some octahedra (labeled as rectangles) are completely deconstructed. Meanwhile, the Eu4 and Eu7 atoms move away from their original positions. This structural change under tensile stress leads to the formation of small cavities. Therefore, the observed crack after amorphization in EuB_6 is likely caused by the tensile stress. It is worth noting that although our results from DFT simulations provide detailed information about the bond breaking and structural failure which initiate the formation of amorphous bands in EuB_6 , the dislocations observed in the experiments cannot be verified in our DFT simulations due to the size limit of structures used in DFT method.

Discussion

Pressure-induced amorphization has been observed in a wide variety of hard and complex crystalline materials including diamond²⁸, ice²⁹, minerals³⁰, semiconductors (Si, Ge, GaAs, InSb)^{31–33}, ceramics (Al_2O_3 , SiC, B_4C , B_6O , Si_3N_4)^{34–37}, and intermetallics (TiNi, Ni_3Al , SmCo_5)³⁸. The formation of amorphization is often related to various mechanisms such as dislocation-induced mechanism³⁹, elastic instabilities⁴⁰, and large plastic shear⁴¹. Similarly, rare-earth hexaborides are a unique class of materials which belong to a strongly correlated electron system comprising high hardness with relatively open structures¹. Thus, conventional plastic deformation associated with motion of

crystal defects is very difficult at room temperature. Therefore, the hexaboride crystalline structures are expected to fail easily on the relative weaker planes to become denser phase under high pressures. Additionally, structural transformations or local softening in the covalent or ionic solid materials are vastly dependent on type of applied pressure conditions. Previous studies on CaB_6 and SrB_6 hexaborides using diamond anvil cell (DAC) experiments under quasi-hydrostatic media demonstrated the polymorphic transition from a simple cubic phase into complex and denser boron network orthorhombic and tetragonal phases^{9,10}, with the assistance of temperature (laser-heating) to produce irreversible bonding for inducing structural transformations. In another study on EuB_6 under hydrostatic high pressures above 20 GPa showed magnetic transitions from ferromagnetic to paramagnetic phase with mixed valence states⁴². Further, temperature-dependent Raman scattering and first-principle calculations showed evidence that the cubic symmetry breaking induces a non-cubic environment in the B_6 octahedron in EuB_6 ¹¹. All these studies performed by hydrostatic or quasi-hydrostatic DAC experiments have not predicted or reported amorphization in hexaborides^{9–11,42}. However, a study by Yan et al.⁴³ reported amorphization in superhard B_4C during depressurization in a non-hydrostatic stress using DAC, while in hydrostatic or quasi-hydrostatic stresses the amorphization was not detected suggesting the nature of the applied stresses play an important role in mechanical instabilities of crystalline structure.

Here we used nanoindentation to induce structural transformations in EuB_6 , which comprises both hydrostatic and non-hydrostatic (shear) stresses. Our TEM observations beneath the indent surface showed that the nano-sized amorphous bands are initiated by dislocations. Such nucleation of dislocations is believed to evolve within the indentation region of a material as the applied load approaches above the critical resolve shear stress (CRSS)^{22,44,45}. The measured angle between indentation surface plane and amorphous slip plane of EuB_6 is $\sim 40\text{--}50^\circ$ suggesting shear stresses play vital role to this process (Fig. 3 and Supplementary Figs. 8 and 9). The DFT simulations further provided evidence of crystal-to-amorphous transition along two major slip systems of EuB_6 . Under pure-shear deformation (Fig. 4 and Supplementary Fig. 10), the B-B bonds in the octahedron is gradually stretched and finally the structure failed initiating the deconstruction of octahedra. While in the biaxial shear deformation⁴⁶ (Fig. 5), the failure is caused directly by breaking of B-B bond within the octahedron of EuB_6 (Fig. 4). This result of biaxial shear is consistent with the bond distortions beneath the residual indent observed by micro-Raman spectroscopy (Fig. 2). However, the tensile deformation of EuB_6 along the $[2\bar{1}2]$ direction shows formation of cavities after the amorphization (Supplementary Fig. 12). Hence, the observed cracks after amorphization is due to the complex stresses (combination of shear and tensile stresses) involved during the indentation. Therefore, our study confirms that the nanoscale amorphous bands in EuB_6 is mediated by the dislocations on relatively easier slip planes by breaking the B-B bond of octahedral B_6 during the shear deformation.

Conclusion

In summary, we employed nanoindentation to investigate the structural transitions in EuB_6 , combining with Raman spectroscopy, Cs-corrected TEM, and DFT simulations. We found localized amorphization in EuB_6 is mediated by dislocations on very specific crystallographic orientations. The simulations indicate that this amorphization process is triggered by breaking B-B chemical bonds in octahedral B_6 upon shear deformation, in line with experimental observations. We believe that our observation

underlying mechanism of shear-induced amorphization mediated by dislocations in a model hexaboride system offers opportunities for controlling the exotic states deformation structures and to tune their properties at high pressures.

Methods

Material fabrication and nanoindentation experiments. The composite B_4C - EuB_6 samples were fabricated using spark plasma sintering (SPS) technique with precursors of Eu_2O_3 ($d_{50} \sim 0.7 \mu\text{m}$, 99% purity) and B_4C ($d_{50} \sim 5 \mu\text{m}$, 99% purity) powders. The powders were wet-milled for 2 h with 150 rpm using planetary ball mill (Fritsch, Germany). Then this ball milled powder was dried in a vacuum oven at 80°C for 3 h. Finally, samples were loaded in an electrically conducting die and consolidated by SPS (Dr. Sinter, Japan) using sintering temperature of 1900°C , held for 15 min with the applied pressure of 45 MPa⁴⁷. The rectangular specimens were cut from the bulk sintered B_4C - EuB_6 composite using slow speed diamond cutter and polished with diamond film sheets i.e., 30, 15, 9, 6, and $1 \mu\text{m}$ for microstructural characterization and nanoindentation tests. Nanoindentation (Hysitron TI950) in load control mode was utilized for determining the mechanical properties of different EuB_6 facets. In this regard, diamond Berkovich tip was used with maximum load of 10 mN held for 2 s. The loading and unloading rates were kept at 1 mN/s. Subsequently, Oliver-Pharr method using the Hysitron TriboIndenter software was used to calculate hardness and Young's modulus from more than 100 indents. Also, a series of indentations at a maximum applied load of ~ 70 mN (with 1000 nm depth) were performed on different EuB_6 facet crystals with MTS G200 system equipped with a Berkovich indenter.

Microstructural characterization. The XRD of as-synthesized samples was obtained by using Ultima IV (Rigaku, Japan) with $\text{Cu K}\alpha$ ($\lambda = 1.5418 \text{ \AA}$), operated at 40 kV and 30 mA. The microstructural analysis of EuB_6 was carried out using SEM (Nova NanoSEM 450 (FEI)). Further, the electron backscattered diffraction (EBSD) patterns were acquired to obtain crystallographic orientation of EuB_6 grains and SEM-EDS was used for elemental mapping analysis. Raman micro spectroscopy was carried out using Renishaw inVia Qontor with an excitation wavelength of 532 nm that has laser beam spot $1 \mu\text{m}$. The cross-sectional TEM specimens underneath the indentation were prepared by standard lift-out technique using focused ion beam (FIB) (VERSA 3D (FEI, USA)) method. The detailed pre- and post-deformation structures were characterized using JEM-ARM 200 F (JEOL, Japan) aberration corrected analytical transmission electron microscope operated at voltage of 200 kV. The SAED patterns were acquired with a camera length of 20 cm. HAADF-STEM images were recorded using an annular-type detector collection semi-angle of $\sim 100\text{--}269$ mrad. STEM-EDS were performed for chemical analysis. The atomic TEM images were simulated using the software package of HREM Research Inc., (Japan). Local strain measurements from HRTEM images of deformation regions have been analysis using peak pair analysis software⁴⁸.

Computational methodology. The DFT calculations were performed using Vienna ab initio simulation package (VASP) with plane wave basis set^{49,50}. The generalized gradient approximation (GGA) type Perdew–Burke–Ernzerhof (PBE) exchange–correlation functional were implemented for electronic exchange and correlation interaction^{51,52}. The pseudopotentials of B and Eu were generated using the projector augmented wave (PAW) method with $2s^2 2p^1$ and $5p^6 6s^2$ treated as valence electrons⁵². The energy cutoff of 500 eV was set in all simulations for the good convergence of energy, force, stress and geometries. The energy convergence of 10^{-6} eV for terminating electronic self-consistent field (SCF) and the force criterion 10^{-3} eV/Å were used in all simulations. A Γ -centered k-point mesh method was used for Brillouin zone integration with the mesh density a high resolution above $2\pi \times 1/40 \text{ \AA}^{-1}$.

For the pure shear and biaxial shear deformations of EuB_6 , we considered $(2\bar{1}2)[120]$ and $(110)[1\bar{1}0]$ as plausible slip systems under both pure and biaxial shear deformation. For shear along $(2\bar{1}2)[120]$ slip system we used a supercell model which contains 63 atoms while we used a 56-atom supercell for $(110)[1\bar{1}0]$ slip system. The $(4 \times 7 \times 3)$ and $(3 \times 9 \times 3)$ K-point meshes were used for $(2\bar{1}2)[120]$ and $(110)[1\bar{1}0]$ shear deformations, respectively. EuB_6 is one of hexaboride compounds and belongs to the space group of $\text{Pm}\bar{3}\text{m}$ in which the unit cell contains one B_6 octahedron and one Eu atom². In each B_6 octahedron, 6 B atoms are covalently bonded to 6 nearby octahedra. Thus, based on Wade's rules⁵³, each B_6 octahedron requires 14 electrons to stabilize the close octahedral structure. In addition, 6 B-B bonds connecting two nearby octahedra also need extra 6 electrons for each octahedron. However, 6 B atoms in each octahedron can only provide 18 electrons. Thus, the Eu atoms are required to transfer 2 electrons to octahedron to satisfy the Wade's rules⁵³.

Data availability

The main data supporting the findings of this study are available within this article and its Supplementary Information. Further data are available from the corresponding author upon request.

Received: 16 September 2021; Accepted: 28 March 2022;
Published online: 22 April 2022

References

- Cahill, J. T. & Graeve, O. A. Hexaborides: a review of structure, synthesis and processing. *J. Mater. Res. Technol.* **8**, 6321–6335 (2019).
- Futamoto, M., Aita, T. & Kawabe, U. Microhardness of hexaboride single crystals. *Mater. Res. Bull.* **14**, 1329–1334 (1979).
- Sun, L. & Wu, Q. Pressure-induced exotic states in rare earth hexaborides. *Rep. Prog. Phys.* **79**, 084503 (2016).
- Erkelens, W. A. C. et al. Neutron scattering study of the antiferroquadrupolar ordering in CeB_6 and $\text{Ce}_{0.75}\text{La}_{0.25}\text{B}_6$. *J. Magn. Magn. Mater.* **63–64**, 61–63 (1987).
- Neupane, M. et al. Surface electronic structure of the topological Kondo-insulator candidate correlated electron system SmB_6 . *Nat. Commun.* **4**, 1–7 (2013).
- Oshima, C., Bannai, E., Tanaka, T. & Kawai, S. Thermionic work function of LaB_6 single crystals and their surfaces. *J. Appl. Phys.* **48**, 3925–3927 (1977).
- Wang, J. et al. High-pressure evolution of unexpected chemical bonding and promising superconducting properties of YB_6 . *J. Phys. Chem. C* **122**, 27820–27828 (2018).
- Tromp, H. J., Van Gelderen, P., Kelly, P. J., Brocks, G. & Bobbert, P. A. CaB_6 : a new semiconducting material for spin electronics. *Phys. Rev. Lett.* **87**, 1–4 (2001).
- Kolmogorov, A. N., Shah, S., Margine, E. R., Kleppe, A. K. & Jephcoat, A. P. Pressure-driven evolution of the covalent network in CaB_6 . *Phys. Rev. Lett.* **109**, 075501 (2012).
- Zhu, L., Borstad, G. M., Cohen, R. E. & Strobel, T. A. Pressure-induced polymorphism in SrB_6 and deformation mechanisms of covalent networks. *Phys. Rev. B* **100**, 214102 (2019).
- Martinho, H. et al. Evidence for a subtle structural symmetry breaking in EuB_6 . *J. Phys. Condens. Matter* **21**, 456007 (2009).
- Duan, L. et al. Pressure induced semiconductor-semimetal-superconductor transition of magnesium hexaborides. *Dalton Trans.* **48**, 14299–14305 (2019).
- Cooley, J., Aronson, M., Sarrao, J. & Fisk, Z. High pressures and ferromagnetic order in EuB_6 . *Phys. Rev. B - Condens. Matter Mater. Phys.* **56**, 14541–14546 (1997).
- Leger, J. M., Rossat-Mignod, J., Kunii, S. & Kasuya, T. High pressure compression of CeB_6 up to 20 GPa. *Solid State Commun.* **54**, 995–997 (1985).
- Wu, X. & Xu, T. T. Measurement of mechanical properties of alkaline-earth metal hexaboride one-dimensional nanostructures by nanoindentation. *J. Mater. Res.* **27**, 1218–1229 (2012).
- Dub, S. N., Kislaya, G. P. & Loboda, P. I. Study of mechanical properties of LaB_6 single crystal by nanoindentation. *J. Superhard Mater.* **35**, 158–165 (2013).
- Zhou, Y., Dai, F., Xiang, H., Liu, B. & Feng, Z. Shear anisotropy: tuning high temperature metal hexaborides from soft to extremely hard. *J. Mater. Sci. Technol.* **33**, 1371–1377 (2017).
- Lundström, T., Lönnberg, B., Törmä, B., Etourneau, J. & Tarascon, J. M. An investigation of the compressibility of LaB_6 and EuB_6 using a high pressure x-ray power diffraction technique. *Phys. Scr.* **26**, 414–416 (1982).
- Sonber, J. K., Murthy, T. S. R. C., Subramanian, C., Hubli, R. C. & Suri, A. K. Synthesis, densification and characterization of EuB_6 . *Int. J. Refract. Met. Hard Mater.* **38**, 67–72 (2013).
- Selvan, R. K., Genish, I., Perelshtein, I., Calderon Moreno, J. M. & Gedanken, A. Single step, low-temperature synthesis of submicron-sized rare earth hexaborides. *J. Phys. Chem. C* **112**, 1795–1802 (2008).
- Wu, P. C. S. Europia as a nuclear control material. *Nucl. Technol.* **39**, 84–94 (1978).
- Schuh, C. A. Nanoindentation studies of materials. *Mater. Today* **9**, 32–40 (2006).
- Cook, R. F. & Pharr, G. M. Direct observation and analysis of indentation cracking in glasses and ceramics. *J. Am. Ceram. Soc.* **73**, 787–817 (1990).
- Udagawa, M. et al. Raman scattering investigation of high temperature ferromagnetic crystals. *J. Phys. Soc. Jpn* **71**, 314–316 (2002).
- Nguyen, T. H. et al. Raman spectroscopic evidence of impurity-induced structural distortion in SmB_6 . *J. Raman Spectrosc.* **50**, 1661–1671 (2019).
- Giannuzzi, L. A. & Stevie, F. A. A review of focused ion beam milling techniques for TEM specimen preparation. *Micron* **30**, 197–204 (1999).
- Reddy, K. M., Liu, P., Hirata, A., Fujita, T. & Chen, M. W. Atomic structure of amorphous shear bands in boron carbide. *Nat. Commun.* **4**, 2483 (2013).
- Pastweka, L., Moser, S., Gumbsch, P. & Mosler, M. Anisotropic mechanical amorphization drives wear in diamond. *Nat. Mater.* **10**, 34–38 (2011).
- Mishima, O., Calvert, L. D. & Whalley, E. ‘Melting ice’ I at 77 K and 10 kbar: a new method of making amorphous solids. *Nature* **310**, 393–395 (1984).
- Samae, V. et al. Stress-induced amorphization triggers deformation in the lithospheric mantle. *Nature* **591**, 82–86 (2021).
- Clarke, D. R., Kroll, M. C., Kirchner, P. D. & Cook, R. F. Amorphization and conductivity of silicon and germanium induced by indentation. *Phys. Rev. Lett.* **60**, 2156–2159 (1988).
- Kailer, A., Nickel, K. G. & Gogotsi, Y. G. Raman microspectroscopy of nanocrystalline and amorphous phases in hardness indentations. *J. Raman Spectrosc.* **30**, 939–946 (1999).
- Zhao, S. et al. Directional amorphization of covalently-bonded solids: a generalized deformation mechanism in extreme loading. *Mater. Today* **49**, 59–67 (2021).
- Schmücker, M., Schneider, H. & Kriven, W. M. Indentation-induced amorphization in mullite single crystals. *J. Am. Ceram. Soc.* **86**, 1821–1822 (2003).
- Chen, M. W., McCauley, J. W. & Hemker, K. J. Shock-Induced localized amorphization in boron carbide. *Science* **299**, 1563–1566 (2003).
- Madhav Reddy, K. et al. Shear amorphization of boron suboxide. *Scr. Mater.* **76**, 9–12 (2014).
- Karre, R. et al. Vacancy-driven shear localization in silicon nitride. *Scr. Mater.* **190**, 163–167 (2021).
- Luo, H. et al. Plasticity without dislocations in a polycrystalline intermetallic. *Nat. Commun.* **10**, 3587 (2019).
- Chen, H., Levitas, V. I. & Xiong, L. Amorphization induced by 60° shuffle dislocation pileup against different grain boundaries in silicon bicrystal under shear. *Acta Mater.* **179**, 287–295 (2019).
- Chen, H., Zarkevich, N. A., Levitas, V. I., Johnson, D. D. & Zhang, X. Fifth-degree elastic energy for predictive continuum stress-strain relations and elastic instabilities under large strain and complex loading in silicon. *npj Comput. Mater.* **6**, 1–8 (2020).
- Levitas, V. I., Ma, Y., Selvi, E., Wu, J. & Patten, J. A. High-density amorphous phase of silicon carbide obtained under large plastic shear and high pressure. *Phys. Rev. B - Condens. Matter Mater. Phys.* **85**, 1–5 (2012).
- Kutelak, L. O. High pressures magnetism of EuB_6 probed with X-ray spectroscopy techniques. (Universidade Estadual de Campinas (UNICAMP). Instituto de Física Gleb Wataghin, 2021).
- Yan, X. Q. et al. Depressurization amorphization of single-crystal boron carbide. *Phys. Rev. Lett.* **102**, 075505 (2009).
- Jang, J. I., Lance, M. J., Wen, S., Tsui, T. Y. & Pharr, G. M. Indentation-induced phase transformations in silicon: Influences of load, rate and indenter angle on the transformation behavior. *Acta Mater.* **53**, 1759–1770 (2005).
- Reddy, K. M. et al. Dislocation-mediated shear amorphization in boron carbide. *Sci. Adv.* **7**, eabc6714 (2021).
- Li, B., Sun, H. & Chen, C. Large indentation strain-stiffening in nanotwinned cubic boron nitride. *Nat. Commun.* **5**, 4965 (2014).
- Sairam, K. et al. Competition between densification and microstructure development during spark plasma sintering of $\text{B}_4\text{C-Eu}_2\text{O}_3$. *J. Am. Ceram. Soc.* **101**, 2516–2526 (2018).
- Galindo, P. L. et al. The peak pairs algorithm for strain mapping from HRTEM images. *Ultramicroscopy* **107**, 1186–1193 (2007).
- Kresse, G. & Furthmüller, J. Efficiency of ab-initio total energy calculations for metals and semiconductors using a plane-wave basis set. *Comput. Mater. Sci.* **6**, 15–50 (1996).
- Kresse, G. & Furthmüller, J. Efficient iterative schemes for ab initio total-energy calculations using a plane-wave basis set. *Phys. Rev. B* **54**, 11169 (1996).
- Kresse, G. & Hafner, J. Ab initio molecular dynamics for liquid metals. *Phys. Rev. B* **47**, 558–561 (1993).
- Kresse, G. & Joubert, D. From ultrasoft pseudopotentials to the projector augmented-wave method. *Phys. Rev. B - Condens. Matter Mater. Phys.* **59**, 1758–1775 (1999).
- Welch, A. J. The significance and impact of Wade’s rules. *Chem. Commun.* **49**, 3615 (2013).

Acknowledgements

We thank Prof. Bikramjit Basu in Materials Research Center at Indian Institute of Science, Bangalore, India for providing sample for this study. The work is financially supported by National Natural Science Foundation of China (Grant Nos. 52150610487 and 51850410501) and seed funding from the School of Materials Science and Engineering at Shanghai Jiao Tong University (China).

Author contributions

K.M.R. conceived and supervised this study. R.K. and Y.H. conducted the mechanical tests and microstructural characterization. K.M.R. performed TEM and STEM characterization. S.S. did nanoindentation and prepared FIB cross-sectioned specimens. S.L. contributed to the Strain mapping analysis. Y.S. and Q.A. conducted the DFT simulations. X.W. participated in discussion. R.K., Y.S., Q.A., and K.M.R. wrote the manuscript. All the authors discussed the results and commented on the manuscript.

Competing interests

The authors declare no competing interests.

Additional information

Supplementary information The online version contains supplementary material available at <https://doi.org/10.1038/s43246-022-00246-2>.

Correspondence and requests for materials should be addressed to Kolan Madhav Reddy.

Peer review information *Communications Materials* thanks the anonymous reviewers for their contribution to the peer review of this work. Primary Handling Editors: Rostislav Hrubíak and Aldo Isidori. Peer reviewer reports are available.

Reprints and permission information is available at <http://www.nature.com/reprints>

Publisher's note Springer Nature remains neutral with regard to jurisdictional claims in published maps and institutional affiliations.



Open Access This article is licensed under a Creative Commons Attribution 4.0 International License, which permits use, sharing, adaptation, distribution and reproduction in any medium or format, as long as you give appropriate credit to the original author(s) and the source, provide a link to the Creative Commons license, and indicate if changes were made. The images or other third party material in this article are included in the article's Creative Commons license, unless indicated otherwise in a credit line to the material. If material is not included in the article's Creative Commons license and your intended use is not permitted by statutory regulation or exceeds the permitted use, you will need to obtain permission directly from the copyright holder. To view a copy of this license, visit <http://creativecommons.org/licenses/by/4.0/>.

© The Author(s) 2022